3-1-2023

Subinertial Sea Surface Heights Anomalies Estimated Using High Frequency Radar Surface Current Data In the Mississippi Bight

Uchenna Nwankwo
University of Southern Mississippi, uchenna.nwankwo@usm.edu

Stephan Howden
University of Southern Mississippi, stephan.howden@usm.edu

Dmitri Nechaev
University of Southern Mississippi, dmitri.nechaev@usm.edu

Brian Dzwonkowski
University of South Alabama, bdzwonkowski@disl.org

JGR Oceans

RESEARCH ARTICLE
10.1029/2022JC019055

Key Points:

- At subinertial scales geostrophic balance is dominant in the Mississippi Bight
- The Least Squares procedure was used to estimate reliable sea level changes on the Mississippi Bight from surface current data
- There are two major patterns of Mississippi Bight sea level gradient determined from EOF

Supporting Information:

Supporting Information may be found in the online version of this article.

Correspondence to:

U. Nwankwo,
uchenna.nwankwo@usm.edu

Citation:

Nwankwo, U., Howden, S., Nechaev, D., & Dzwonkowski, B. (2023). Subinertial sea surface heights anomalies estimated using high frequency radar surface current data in the Mississippi Bight. *Journal of Geophysical Research: Oceans*, *128*, e2022JC019055. https://doi.org/10.1029/2022JC019055

Received 2 JUL 2022
Accepted 10 FEB 2023

Subinertial Sea Surface Heights Anomalies Estimated Using High Frequency Radar Surface Current Data in the Mississippi Bight

Uchenna Nwankwo[1], Stephan Howden[1], Dmitri Nechaev[1], and Brian Dzwonkowski[2]

[1]School of Ocean Science and Engineering, Hydrographic Science Research Center, The University of Southern Mississippi, Hattiesburg, MS, USA, [2]University of South Alabama, Dauphin Island Sea Lab, Mobile, AL, USA

Abstract Sea level studies in the Mississippi Bight (MSB) are less abundant than in other coastal waters of USA. This study investigates the subinertial (time scales >2 days) sea level anomalies in the MSB shelf. The diagnostics of the terms in the invariant form of the momentum equation were computed to determine which terms have the most influence on the anomalies in sea level. It was determined that at subinertial scales the geostrophic balance is the dominant balance in the MSB while the non-linear and time derivative terms are insignificant relative to the Coriolis term. A Least Squares procedure was applied to the subinertial surface currents data from high frequency radar surface currents (filtered with a window of 2-day Butterworth filter) to extract subinertial sea level anomalies in the MSB shelf using both geostrophic balance and the invariant form of Reynolds' averaged momentum equations. The resulting subinertial sea level anomalies were validated using sea level observations from an offshore buoy and Sentinel-3 along-track satellite altimeter data. The estimated sea level anomalies were reasonably close to observations (more than half had root mean square difference of <0.04 m) and mostly influenced by geostrophic balance. Analysis of the empirical orthogonal functions showed that the first two modes explained the majority (85%) of the variance in the sea level anomalies estimated using the geostrophic approximation. Absolute sea level could be estimated if Global Navigation Satellite System buoys are deployed in the radar footprint.

Plain Language Summary Compared to other USA coastal waters, fewer sea level studies have been conducted in the Mississippi Bight (MSB). This study focuses on slow varying sea level anomalies with periods longer than 2 days. The terms in the equation governing the circulation in the MSB were evaluated using high frequency (HF) radar velocity data to determine which terms contributed the most to the sea level anomalies. The study demonstrated that the term associated to Earth's rotation has the largest amplitude implying that the dominant balance is between this term and the term related to sea level slope. Sea level anomalies estimated from both this dominant balance and the full governing equation by applying a Least Squares procedure. Buoy and Sentinel-3 satellite altimeter sea level observations were used not only to validate the estimated sea level anomalies but also to confirm the validity of the dominant balance. Two major patterns of sea level spatiotemporal variability were determined. They accounted for 85% of the changes in the sea level anomalies. Additional observations within the HF radar coverage area such as high quality positioning data could be used to reference the estimated sea level anomalies.

1. Introduction

To a first order approximation, there is a geostrophic flow in the ocean interior where temporal Rossby, Rossby and Ekman numbers are assumed to be small. The barotropic component of this flow results from the balance between the horizontal components of the Coriolis and pressure gradient forces where pressure gradients result from gradient in sea level (Cushman-Roisin & Beckers, 2012). Typically, the subinertial (defined here as timescales greater than 2-day) sea level gradient in the open ocean can be attributed to changes of currents in accordance with geostrophic balance. However, the dominance of the geostrophic balance becomes less certain on continental shelves (Lentz & Fewings, 2012). This is partly due to the varying bathymetry and stratification, both of which can contribute to the separation or overlap of the surface and bottom boundary layers (Lentz & Fewings, 2012), as well as the prevalence of high frequency (HF) non-linear processes (e.g., surface gravity waves; Woodworth et al., 2019). These changes in ocean dynamics complicates continental shelf processes

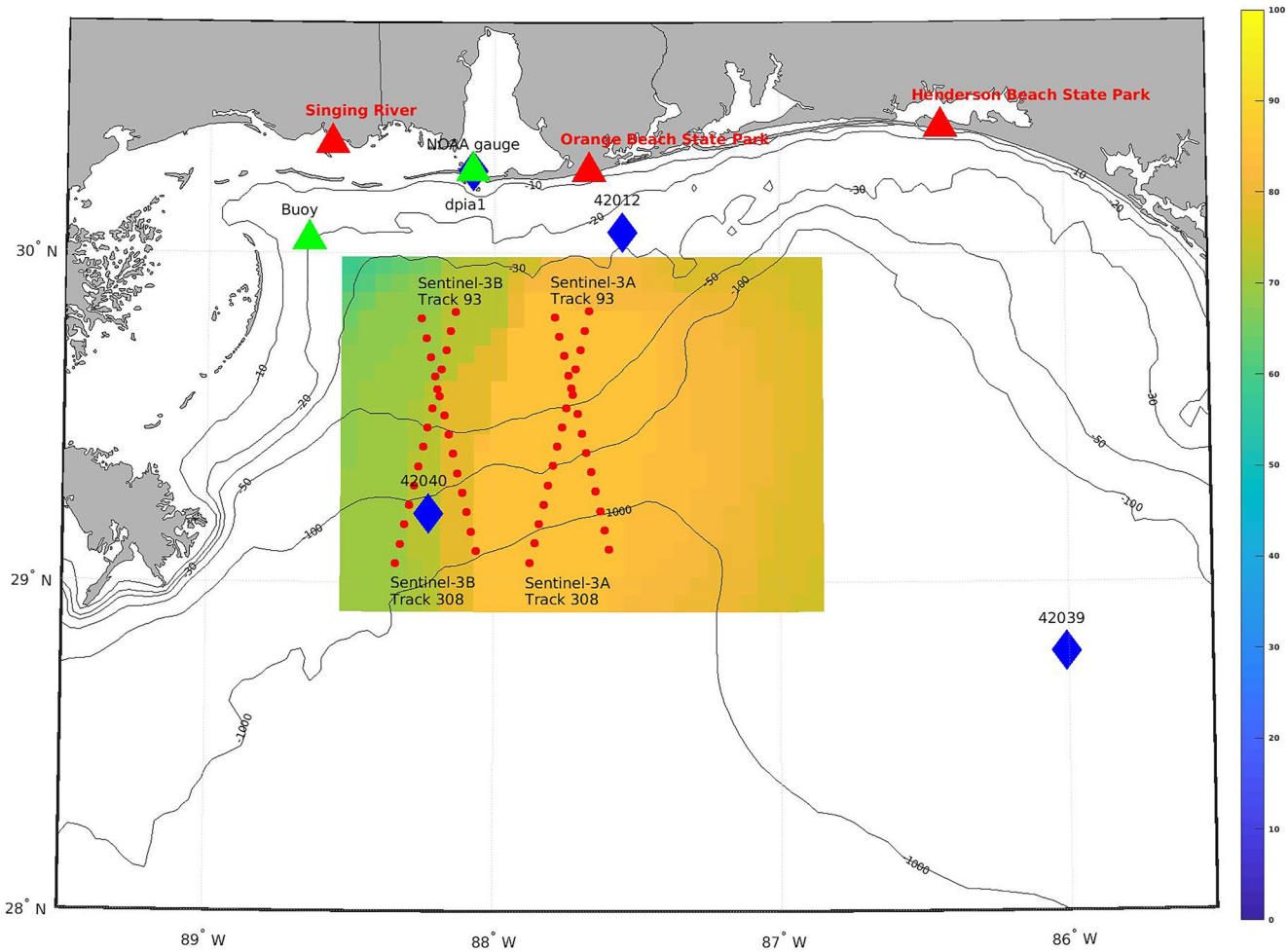

Figure 1. Map of the study region with surface current coverage domain (color plot) showing percentage of HFR data availability. The blue diamonds represent the locations of wind stations; starting from the northmost and moving in the clockwise direction dpia1 (in a similar location with the northmost green triangle), 42012, 42039, and 42040. The ~5 MHz HFR stations locations are represented by red triangles; starting from the leftmost Singing River Island in Mississippi, Orange Beach in Alabama and Henderson Beach State Park in Florida. Green triangles represent the locations of the sea level stations: coastal gauge (NOAA 8735180 Dauphin Island) and offshore buoy. The first X-crossing is S3B pass 93 and 308 while the second X-crossing is S3A pass 93 and 308.

(Dzwonkowski & Park, 2012). As such, in addition to geostrophic sea level gradient, ageostrophic dynamics can contribute to subinertial sea level gradient on the shelf.

The contributions of oceanographic processes to gradients in sea level differ for different temporal and spatial scales. Many sea level studies have focused on temporal anomalies, but spatial gradients in sea level have been challenging to observe on the shelf, since altimeters have sparse spatial coverage and require special processing on the shelf. Studies of both temporal and spatial sea level gradients can be useful in understanding of the roles of oceanographic processes to sea level gradients (Woodworth et al., 2019). Particularly, in the Mississippi Bight (MSB) (Figure 1) of the Northern Gulf of Mexico shelf (nGOMs), such studies have been limited (MSB extends from the shoreline to the shelf break).

Previous studies in the MSB have focused more on shelf circulation, resulting in only a few studies on sea level gradients. Ohlmann et al. (2001) used satellite altimetry data to investigate mean flows on the shelf rise area of the GOM and determined that the contribution of eddy-generated vorticity flux to mean flow competes with the contributions of wind stress curl. Though they estimated sea level gradients due to eddies, these results were generally at the outer edge of the shelf. On seasonal timescales, Dzwonkowski and Park (2010) using depth integrated velocities from a single moored Acoustic Doppler Current Profiler (ADCP) at the 20 m isobaths offshore of Mobile Bay, observed an eastward flow in the late spring/early summer, which they suspected resulted from a

barotropic pressure gradient and westward flow in the late fall/early winter, which resulted from the wind driven current. While at synoptic timescales (i.e., days to weeks), Dzwonkowski and Park (2012) observed a relationship in the variability of coastal sea level and variability of wind as it transitions back and forth between upwelling favorable and downwelling favorable. However, their study was limited to coastal sea level measurements with no consideration of the sea level over the broader shelf. Valle-Levinson and Martin (2020) used coastal sea level measurements to determine the solar and lunar contributions to sea level variability at interannual time scales along the coastal region of the nGOM.

Several techniques are available for sea level measurements, each with their own strengths and weaknesses. In coastal regions, sea level is measured using a variety of instrumentation, most of which measure sea level relative to land. These instruments are installed on relatively stable platforms like piers. However, they provide measurements mostly near-shore, at single points and are not evenly distributed. Offshore sea level can be measured using bottom-mounted pressure sensors (with a correction for atmospheric pressure) and/or Global Navigation Satellite System (GNSS) installed on buoys (Bisnath et al., 2004; Nwankwo et al., 2019). Sea level observations utilizing GNSS receivers on buoys can be approximated to be from a single point like in coastal tide gauges and staffs and provide absolute (e.g., geodetic) sea level measurements. Sea level observations from these single point stations (tide gauges and buoys) are usually at high temporal resolutions (seconds-hours intervals) (Nwankwo et al., 2019).

Estimates of coastal and offshore sea level heights and anomalies can also be estimated from satellite altimetry data and numerical models. Along-track Jason and Topex/Poseidon data are at 7 km intervals, having maximum track spacing of about 300 km and temporal resolution of 10-day. Along-track satellite altimetry data are interpolated to generate sea level data on a regular spatial grid (Ohlmann et al., 2001). In the case of gridded altimetry data, the spatial resolutions are large (Chavanne & Klein, 2010) for instance, 30 km × 30 km (Roesler et al., 2013).

Though satellite altimeters are able to provide estimates of wide areas of absolute sea level (at poor temporal and spatial resolutions), they perform poorly during heavy-rain events (>12 mm hr-1), under low and complex winds and in the presence of surface slicks patches due to calm surfaces (Quartly et al., 1998; Roesler et al., 2013; Tournadre et al., 2006). Chelton et al. (2001) enumerated various drifts and calibrations required for satellite altimetry data. For instance, the measurement system drift is calibrated using tide gauges. Christensen et al. (1994) argued that the drift in satellite altimeter measurements system results from the in-situ tide gauges used in the calibration noting that the tide gauges are vulnerable to subsidence or uplift due to isostatic rebound. Chelton et al. (2001) proposed the use of Global Positioning System (GPS) buoys for calibrating the altimeter measurement system. However, the technique is expensive as it requires the deployment as well as maintenance of several GPS buoys along the tracks of the altimeters. Additionally, the integrity of the geophysical corrections applied to altimeter data degrades in the shelf region because shoaling of bathymetry induces more variability in physical processes such as tides (Andersen & Scharroo, 2011). Furthermore, satellite altimeter waveforms are not reliable when the foot print of satellite altimeter such as Jason-2 is closer than 25 km to the coast (Roesler et al., 2013). Rudnick et al. (2014) noted that numerical models such as the Princeton Ocean Model assimilates sea level data from satellite altimetry data. As such, coastal sea level outputs from such models could be degraded when poor quality satellite altimeter data are assimilated. Therefore, there is need for adequate in-situ sea level data on the continental shelf and coastal regions.

A potential alternative to satellite altimetry based measurement of sea level anomalies over shelf regions is using sea level estimates based on currents derived from high frequency radar (HFR). Differential sea level anomalies can be estimated using surface currents data derived from HFR but they do not have an absolute reference like in satellite altimetry. Roesler et al. (2013) used such a method to investigate the validity of different satellite altimetry retrackers (models used to determine the offset of echoes in order to estimate satellite range above the sea surface) close to the coast of California. The same method was also used by Chavanne and Klein (2010) to confirm that sub-mesoscale processes were present in satellite altimetry along-track data.

Given the successes of these previous studies in using HFR to estimate sea level anomalies as well as the limited scope of the previous circulation studies in this region, this paper seeks to improve the understanding of the subinertial sea level anomalies on the shelf of the MBS. In this context, without an ability to absolutely reference sea level derived from surface velocities, sea level anomalies are computed at each observation time from the spatial averaged derived sea level. Note that from one observation time to another the anomalies are, in general, with

respect to a different mean value. This is the first study to use HFR to conduct a large-scale sea level anomalies analysis in the MSB. While the idea of using HFR surface current data to estimate sea level anomalies is not new, a novel technique involving the Least Squares adjustment was adopted in estimating the anomalies in sea level. Diagnostic analysis of the terms in the momentum equation was conducted to investigate if the subinertial MSB sea level anomalies were mainly due to geostrophically balanced currents. Dominant modes in the estimated subinertial sea level anomalies were analyzed using empirical orthogonal functions. Subinertial sea level anomalies are hereinafter referred to as sea level anomalies. Details of the data used and the various data processing techniques applied are discussed in Section 2. The following data analyses were presented in Section 3: spectral analysis of filtered and unfiltered currents, diagnostics of the terms in the momentum equation, extraction of sea level using Least Squares technique and estimation EOF of the sea level anomalies. Results of the momentum equation diagnostics, estimated HFR sea level anomalies, comparisons of the HFR sea level anomalies to the sea level anomalies determined from other sources (coastal sea level gauges, offshore buoy and satellite altimeter) and the HFR sea level anomalies EOF modes were presented in Section 4. In Section 5, the results of the analysis are discussed and conclusions from the study are summarized in Section 6.

2. Data and Data Processing

2.1. HFR Data

In general, HFR systems are broadly divided based on the antenna configuration (direction finding and phase-array) and the processes involved in estimating surface currents using both systems are similar and were discussed in Paduan and Graber (1997). Summarily, it involves the transmission of vertically polarized HF radio signal, backscatter of the signal by Bragg waves (waves satisfying the Bragg condition: wavelengths are half the wavelength of the transmitted signal) and reception of the signals backscattered toward the antenna. The system then estimates range to the scattering waves, bearing of the received signals, signal-to-noise ratio of the signals and Doppler shift (Teague et al., 1997). The estimated Doppler shift corresponds to the Doppler Effect due to the ambient ocean currents and Bragg waves. By eliminating the Doppler Effect due to the Bragg waves, known from the deep water wave dispersion relation, the remainder of the Doppler shift is due to the ambient ocean currents. The remaining Doppler shift is multiplied by the wavelength of the Bragg wave resulting in radial surface currents toward or away from the radar. The effective water column depth of the estimated radial surface currents depends on the wavelength of the HFR signal (Stewart & Joy, 1974) and the current profile below the surface. Because a single HFR only gives information on the component of currents moving toward or away from a given range cell ("radials"), the total velocities of the surface current are determined by combining the estimated radial currents at angular intersection greater than 30° but less than 150° from at least two neighboring HFR stations (Paduan & Graber, 1997).

The Central Gulf of Mexico Ocean Observing System (CenGOOS) at the University of Southern Mississippi (USM) is a part of the Gulf of Mexico Coastal Ocean Observing System (GCOOS). CenGOOS uses CODAR Seasonde systems which are long (5 MHz) and short (25 MHz) range HFRs in the northern Gulf of Mexico. The emphasis of this study is the domain covered by the long range HFR having 1-hr temporal resolution and a spatial resolution of ∼6 km (Figure 1). The radial data generated from these long range HFR stations corresponds to currents of the surface water column of an effective depth of ∼2 m (Stewart & Joy, 1974).

The HFR data have gaps for various reasons. For example, if tropical storm force winds are forecasted to strike a station within 72 hr, the station is removed and this disrupts surface current observation as noted in Nwankwo et al. (2020) for the analysis of Hurricane Nate. Furthermore, calm seas have few waves to backscatter transmitted signals (Liu et al., 2010). System malfunctions at the HFR stations also disrupts observations and there are limited number of stations in the MSB as shown in Figure 1. Some of these issues can be significantly reduced by having redundant HFR stations as found on the California shelf (Roesler et al., 2013). Despite the limitations of the HFR network in the MSB, extensive data has been collected over the MSB region.

Surface velocity vectors are generated using the estimated surface current radials. This process was conducted using the MATLAB programs (hfrprogs toolbox) available from the Radio Operators Working Group (ROWG). Various efforts have been made to quality control the data associated with this network. Velocity uncertainties included the Geometric Dilution of Precision (GDOP) are computed from the angle of intersection of surface current radials used to estimate total surface current vectors. While Hode (2019) eliminated velocity data whose

uncertainties that were greater than 0.05 m/s, this constraint was relaxed depending on the situation as velocities whose uncertainties that were less than 0.2 m/s were accepted for hurricane periods. Using a 0.05 m/s constraint resulted in prohibitively large data gaps. As a result of this, 0.1 m/s constraint was adopted as a trade-off between accuracy and data availability. It should be noted that this was still a conservative choice as higher HFR data uncertainties have been reported in other studies (Chapman & Graber, 1997; Yoshikawa et al., 2006). After evaluating the data over the life time of the network, the period of 1 February 2016 to 30 November 2019 was selected for the analyses in this study.

Surface current data availability varied with space and time. Color plot in Figure 1 showed that the percentage of the surface current data was highest in the mid-region of the three HFR stations as it is the region where the signals from the three HFR stations had a 100% overlap. However, the percentage of data availability declined away from this region due to lack of redundancy in HFR coverage. In cases where data were available in at least three data points that are one grid step in space and time from a missing data point, nearest neighbor averaging interpolation technique was used to fill the missing data point. Other data gaps were interpolated using a Gauss-Markov estimator (Appendix section A) which is a statistical technique similar to the interpolation technique applied in Cho et al. (1998). However, in cases of insufficient data or lack of data around a data gap to build an adequate statistic, the data gap interpolations were ignored. Insufficiency or lack of data was mostly due to system removal or malfunction.

2.2. Satellite Altimetry Data

Sentinel 3A (S3A) and 3B (S3B) along-track sea surface height anomaly (SSHA) data were used in this study. The following corrections had been applied to the datasets: long wavelength error, ocean tide and dynamic atmospheric forcing (Mertz et al., 2017). S3A along-track data that were investigated spanned from February 2016 to November 2019 while S3B along-track data spanned a shorter period from December 2018 to November 2019 given that the S3B satellite was launched 2 years (2018) after the launching of S3A satellite. The SSHA from the S3 along-track data was used because it has a better spatial resolution (~7 km) compared to the gridded satellite altimeter products. Unlike other satellite altimeter missions such as Topex/Poseidon and Jason, S3 estimates sea surface height in the synthetic aperture radar mode and it provides more reliable results in coastal regions (Bonnefond et al., 2018). Tracks 93 and 308 of the orbits of both S3 satellites pass the HFR domain in the north-south orientation (Figure 1) each with a repeat period of 27 days thereby ensuring at least monthly data availability over the HFR domain for each track. Both tracks (93 and 308) have an interval of 7 days and track 93 of S3A lags track 93 of S3B by 17 days as well as for track 308.

2.3. Sea Level Gauge Data

Regional coastal and offshore sea level data were analyzed for this study. The coastal station used in this study was the National Oceanic and Atmospheric Administration (NOAA) National Sea level Observation Network (NWLON) gauge (8735180) at Dauphin Island, Alabama. The sea level sampling data interval at the gauge is 6 min. Sea level data, downloaded from the coastal station was with respect to the station gauge zero. In addition to the sea level data, atmospheric pressure data were also downloaded from the station so as to correct for inverted barometric effect. Unlike in the sea level data, there were several months of data gaps in the atmospheric pressure data. Some of the data gaps were filled with data from a nearby meteorological station (8734673) at National Data Buoy Center (NDBC) Fort Morgan, Alabama.

Offshore sea level data was from a buoy deployed by USM at the 20 m isobath on the Mississippi shelf. Several sensors were installed on the buoy and they include but are not limited to a Trimble NetRS GNSS receiver and antenna. Sensors on the buoy were operational until the eye of Hurricane Nate in 2017 passed at ~40 km to the west of buoy. However, the GNSS sensor survived the hurricane and remained operational until the buoy was retrieved. Sea level data obtained using the ellipsoidal height from the GNSS antenna were referenced to the North American Datum 1983, National Adjustment 2011 (NAD83(2011)). The data had been used to estimate the storm surge at the buoy location in comparison to that at a coastal sea level gauge (Nwankwo et al., 2020). Hence, the buoy data was considered viable in estimating MSB sea level anomalies. Atmospheric pressure data from the closest NOAA station (8735180 at Dauphin Island) was used for correcting for inverted barometric effect at the buoy location.

2.4. Wind Data

Given that wind influences the currents in the MSB, local wind data of the same time period as the surface current data were analyzed. There were inconsistences in wind data sampling intervals on the various stations; at some stations (dpia1h and 42039) the wind data were at 1-hr intervals while at the other stations (42012h and 42040h), the data were at 1-hr intervals in some periods and at 10-min intervals in other periods. At the stations where the wind data were at 10-min intervals, they were subsampled to 1-hr intervals by averaging 1-hr data about the hour mark. An optimal wind data was estimated using the various wind data (Appendix Section B). Gaps in the optimal wind were interpolated using a method similar to (Dzwonkowski et al., 2009; Liu & Weisberg, 2007).

3. Data Analysis

3.1. Time Averaging and Power Spectra (Temporal Spectral Analysis)

An adequate filtering technique was required to extract the subinertial components from the surface currents, coastal and buoy water level and atmospheric pressure data. A second order Butterworth filter, which eliminates phases shift by filtering in the forward and backward directions, was adopted. Considering the presence of data gaps, the filter was applied to only available data that were continuous in time intervals.

The decision on the temporal averaging period used in the low pass filter was dependent on the near-inertial frequency of the MSB as well as spatial scales. Processes whose spatial scales are smaller than the internal Rossby Radius of Deformation (RRD) in the MSB and at the same time have frequencies which are higher than the MSB inertial frequency are not influenced by the Coriolis force (Cushman-Roisin & Beckers, 2012). Chelton et al. (1998) while accounting for stratification, earth rotation and water depth estimated the internal RRD for the GOM to be ∼40 km while also noting that the RRD varies by <10 km. MSB is in the vicinity of the critical latitude (30°N) which makes inertial period to coincide with diurnal period. Cushman-Roisin and Beckers (2012) suggested that in estimating temporal averages, the averaging period should be at least over the period of the processes which are not of interest, adequate for obtaining statistical mean but short enough so that the evolution of the processes of interest should be captured. A cut-off period of 2 days was adopted to low-pass filter the surface currents on all the grid points resulting in the low frequency subinertial surface currents (Chavanne & Klein, 2010; Liu & Weisberg, 2007). This thereby eliminates HF processes like semidiurnal and diurnal tides and inertial motions as noted by Roesler et al. (2013).

The same filtering technique was applied to both coastal and buoy sea level and atmospheric pressure data. The resulting subinertial coastal and buoy sea level data were subsequently corrected for inverted barometric effect using the corresponding subinertial air pressure data and adopting the formula in Pugh and Philip (2014). Considering that the sea level from the coastal and buoy stations had different references, the temporal means of the individual subinertial sea level were subtracted from each corresponding subinertial sea level to estimate anomalies similar to Rudnick et al. (2014).

Spectral analysis was conducted to investigate the efficacy of the Butterworth filter in reducing HF energies. Figure S1 in Supporting Information S1 displays the spatially averaged total spectra computed from ∼50% of the velocity grid points corresponding to continuous data availability in both the raw and filtered data spanning from 10 October 2016 to 10 December 2016. The time frame was chosen because it was the longest window of continuous data in time. The reported frequencies are from the first frequency bin to the Nyquist frequency bin. The zeroth frequency bin was not present because the time mean was removed in the pre-whitening process. Uncertainties in the computed mean spectrum for the respective frequency bins are shown by standard deviation error bars. The spectra show that the filter mitigates the energies of HF signals while preserving the energies in low frequency signals; observe the divergence in the raw and filtered spectral at scales less than the subinertial scale.

3.2. Momentum Equation Terms Diagnostics

The momentum equations are used to diagnose ocean dynamics. Magnitudes of the terms in the equations can vary depending on the temporal and spatial scales of processes under consideration. Through the diagnostics of the terms in the momentum equation, the relative significance of the individual terms in the equations is estimated. For this study, the data available for the diagnostics of the terms includes the subinertial surface current velocities and the corresponding velocity anomalies as well as the wind data. Different version of the primitive

momentum equations were used in the diagnostics of terms. In Madec et al. (1998), the advective terms in the primitive momentum equations were replaced by the sum of the Lamb vector and the gradient of kinetic energy resulting in the invariant form of the momentum equations. Ohlmann et al. (2001), neglected the time derivative term in the invariant form of the Reynolds' averaged momentum equations they presented where the gradient of kinetic energy and Lamb vector terms produced pair of "mean/subinertial" and "turbulent" terms. In their equation, the Lamb vector involved only the z-component of relative vorticity. By restoring the time derivative term, the resulting equation (Equation 1) was adopted to investigate the contribution of different terms to subinertial sea level. Hereinafter the terms involving the z-component of relative vorticity will referred to as vorticity terms.

$$\frac{\partial \overline{\mathbf{u}}}{\partial t} + \left(\overline{\xi} + f\right)\hat{\mathbf{k}} \times \overline{\mathbf{u}} + \hat{\mathbf{k}} \times \left(\overline{\xi' \mathbf{u}'}\right) = -\nabla\left(g\,\overline{\eta} + \frac{1}{2}\,\overline{\mathbf{u}'.\mathbf{u}'} + \frac{1}{2}\,\overline{\mathbf{u}}.\overline{\mathbf{u}}\right) + \frac{\partial \sigma}{\partial z} \tag{1}$$

where $\overline{\mathbf{u}}$ corresponds to the horizontal velocity of subinertial surface currents, $\mathbf{u}'$ is horizontal perturbation velocity estimated from the differences between the velocity of the unfiltered and subinertial surface currents, $\overline{\xi}$ is the vertical component of relative vorticity estimated using the subinertial currents $\overline{\xi} = \left(\frac{\partial v}{\partial x} - \frac{\partial u}{\partial y}\right)$, ξ' is perturbation of the vertical component of relative vorticity estimated using the perturbation velocity $\xi' = \left(\frac{\partial v'}{\partial x} - \frac{\partial u'}{\partial y}\right)$, f is the Coriolis parameter, $\overline{\eta}$ is subinertial sea level anomalies, g is gravity acceleration, $\frac{\partial \sigma}{\partial z}$ is the most important part of the divergence of turbulent viscous stresses in the upper boundary layer, $\hat{\mathbf{k}}$ is the vertical unit vector and $\times$ denotes the vector (cross) product. Hereinafter x and y momentum equations will be referred to as along-shelf and across-shelf momentum equations, respectively and they correspond to the east-west and north-south orientations, respectively, using similar conventions as Dzwonkowski and Park (2012). Terms with overbars involving the product of perturbations such as $\left(\overline{\xi' \mathbf{u}'}\right)$ were filtered using the same technique as the filtering of the surface currents.

Several assumptions were made in (Equation 1). Perturbation velocity components were obtained based on the assumption that the 2-day filtering of velocity obeys the Reynolds axioms. The divergence of turbulent viscous stress was approximated by the quotient of wind stresses and the boundary layer depth estimate d. Here the units of the kinematic wind stress components τ_x and τ_y referred to in the along-shelf and across momentum equations is $\frac{m^2}{s^2}$. Furthermore, as it is commonly assumed in boundary layer consideration (Bretherton, 2002), the terms representing divergence of the Reynolds fluxes accounted only for the vertical shear of horizontal velocity. Other assumptions includes f-plane, Boussinesq and Hydrostatic approximations. Under the hydrostatic approximation, the baroclinic effect enters the momentum equations in the horizontal component of momentum via horizontal pressure gradient. Since the equations are written for a very thin upper layer of the ocean, the effects of density anomaly on pressure are negligible. There was no separation of the flow into barotropic and baroclinic components. Similar approach was adopted in Chavanne and Klein (2010) to estimate sea level changes.

Besides the sea level gradient term, each term in Equation (1) can be estimated with the available data. Using the subinertial surface currents, the time derivative, mean vertical component of relative vorticity and gradient of mean kinetic energy terms were computed. The perturbation of the vertical component of relative vorticity and kinetic energy of perturbation were computed using the residual in the difference between the original and subinertial surface currents. The wind data was used to estimate wind stress at the surface using Large and Pond (1981) formula which resulted in the kinematic wind stress.

The geostrophically balanced dynamics of the subinertial flow in the MSB assumes that the leading terms in Equation (1) are the Coriolis acceleration and the pressure gradient force due to the slope of the sea level as shown in Equation (2):

$$f\hat{\mathbf{k}} \times \mathbf{u} = -g\nabla\eta \tag{2}$$

where f is the Coriolis parameter, u is the geostrophic velocity vector, $\nabla\eta$ is the sea level gradient and g is the gravity acceleration. Conventionally, it is assumed that for this balance to hold in the MSB, the Rossby number (R_o) (ratio of relative vorticity and Coriolis parameter Chavanne & Klein, 2010) must be less than 0.1 (Kim, 2010). $R_o < 0.1$, indicating that the Coriolis term in Equation (1) is the dominant term given that the advective time scale defines the scale of the time derivative term. Furthermore, the spatial scales of the dominant currents must be greater than the internal RRD. Although the spatial scale of the study region is greater than

the MSB internal RRD value (40 ± 10 km) that did not guarantee that Equation (2) adequately represented the dynamics that results in anomalies in sea level in the MSB.

3.3. Estimates of Sea Level and Sea Level Anomalies

To investigate if Equation (2) represented the dynamics that results in the MSB sea level anomalies, a Least Squares adjustment technique was implemented to estimate sea level fields at each observation time, minimizing the squared residual in Equation (2). Note that these sea level estimates are indeterminate to a reference level. For a two-dimensional velocity vector field, the u and v components can be rewritten using two scalar functions: stream function and potential, describing the rotational (non-divergent) and potential parts of the velocity field, respectively. Sea level estimated using the geostrophic approximation Equation (2) corresponded to the non-divergent part of the subinertial surface currents. The reconstructed sea level minimizes the cost function (Equation (3)) using a Quasi-Newton with a Limited-Memory Broyden–Fletcher–Goldfarb–Shanno (LBFGS), optimization algorithm

$$J = 0.5 \sum \mathrm{W}_1(\mathrm{g}\nabla\eta + \mathbf{U})^2 + 0.5 \sum \mathrm{W}_2(\Delta\eta)^2 \tag{3}$$

where $\boldsymbol{J}$ is comprised of two terms: a "data term", where $\mathrm{g}\nabla\eta$ is the finite-difference approximation of the pressure gradient, and $\mathbf{U}$ is the left hand side of Equation (2) and a smoothness term, where $\boldsymbol{\Delta\eta}$ is the finite-difference Laplacian of the sea level. The summation goes over all grid points where $\mathbf{U}$ is available for the first term of the cost function and over all grid points where Laplacian of the sea level is computed. The smoothness term is introduced to penalize grid-scale sea level variations and to produce a smooth interpolation of sea level to the regions where data gaps were present. The data term weight W_1 and the smoothness term weight W_2 are represented by diagonal matrices. The diagonal weight matrices (W_1 and W_2) in Equation (3) were defined using a deterministic procedure. W_1 was initially set to be a unit matrix. Using this matrix, the cost function was evaluated for the flat sea level field and the resulting cost function value with units $\left(\frac{\mathrm{m}}{\mathrm{s}^2}\right)^2$ was used to normalize W_1. This normalization did not affect the result of the optimization because the cost function is defined up to an arbitrary multiplicative factor. W_2 was also initialized as a unit matrix scaled with the ratio of the nominal value for the first term of the cost function and the second term of the cost function evaluated for an analytical grid scale oscillating field. As such, the units of W_2 were inverse of the units of the squared Laplacian term which automatically makes the second term of the cost function unitless. This initial scaling did not mitigate small-scale features in the estimated sea level. The optimal weight of the smoothing term was determined by conducting a set of Least Squares experiments with a range of weights of the smoothness term. Real data were used in the experiments. At the end of each experiment, the first and second terms of the cost function were determined. Both the first and second terms of the cost function increased as the weight of W_2 increased. The optimal weight W_2 corresponded to the Least Squares fit where small-scale sea level features were filtered while the increase of the first term of the cost function was less than 10% of the first term of the cost function value for W_2 equal zero.

The above Least Squares technique of estimating sea level differ from the Optimal Interpolation technique adopted in Roesler et al. (2013). While the Optimal Interpolation technique is a statistical approach and requires prior knowledge of data and background error covariances, the Least Square technique is a deterministic approach and does not require prior knowledge of the error covariances. Roesler et al. (2013), applied an amplification factor to their optimal interpolation estimated HFR SSHA to correspond to satellite altimeter SSHA. This amplification factor was not required in the HFR SSHA estimated in this study.

Before the application of the Least Squares technique, the technique was used to reconstruct an analytical sea level field using an analytical velocity field while considering cases of data gaps in the current data. Due to the indeterminacy of the reconstruction sea level to reference level, an anomaly field with respect to the spatial mean was computed for both the reconstructed and analytical sea level fields for comparison. The accuracy of the reconstructed field (norm of the difference between the reconstructed anomalies in sea level and the analytical sea level anomalies) was at the millimeter level when 30% of data gaps were present in the analytical current field. It was much smaller than 1 mm when 0% of data gap was considered.

Sea level was only reconstructed if gaps in the domain were less than 25% of the total data points to ensure that sufficient amount of data were available for estimating sea level anomalies across the domain. For all estimated

sea level, the spatial mean across the domain was subtracted so that the anomalies had a zero spatial mean. Hereafter, we will refer to the reconstructed sea level anomalies as HFR SSHA.

Uncertainties in the geostrophic HFR SSHA were determined using an ensemble approach. This approach involves random perturbation of observations to generate ensembles of data realizations. An ensemble approach was adopted in several studies for estimation of background error covariance models (e.g., Pereira & Berre, 2006; Zagar et al., 2004). Errors in the radial surface currents data were assumed to be uncorrelated. For each radial data used to generate surface current vectors, an ensemble of realizations was randomly generated using random normal numbers with zero mean and standard deviation was assigned the value of the error corresponding to the radial data. All the procedures undertaken to arrive at HFR SSHA were repeated for all the simulated realizations of data. Ensemble mean and standard deviations were computed to estimate the HFR SSHA uncertainties for each grid point. The maximum estimated standard deviation (0.01 m) was adopted as the geostrophic HFR SSHA uncertainty and it was more pronounced near the boundary of the domain where there are the most data gaps (Figure 1).

3.4. Empirical Orthogonal Functions

Spatial and temporal patterns in the estimated HFR SSHA using Equation (3) were analyzed using EOF. The field of SSHA was setup to correspond to the S-mode analyses which involves the re-arrangement of the sea level data into a 2-dimensional matrix where the columns of the matrix correspond to the geodetic positions of the domain grid points while the rows correspond to time (Björnsson et al., 1997). Temporal means of each column were removed and the result was used to form a covariance matrix. The eigenvectors (empirical modes) of the covariance matrix corresponding to the two largest eigenvalues were extracted. Evolution of the various empirical modes was determined through the resulting principal component.

4. Results

4.1. Momentum Equation Terms Diagnostics

For quantitative analysis of the applicability of Equation (1) in the MSB the terms in Equation (1) were evaluated for every internal grid point of the domain. Statistical analysis of each term from the results of the diagnostics was computed over the entire time series. The statistics comprised of the mean and standard deviation values of the individual terms corresponding to the along-shelf and across-shelf momentum equations across the domain (supporting document S2, S3, S6, and S74). Table 1 was used to summarize these results by representing the statistics of the various terms over the entire time and space.

The relative importance of the individual terms in the along-shelf momentum equation were determined from the mean and standard deviation of the terms as shown in Table 1 and Figure S2 in Supporting Information S1. Note that the red line (zero contour) on the plots shows the transition from positive to negative values. Absolute values of the mean for individual terms were considered to focus on their magnitudes. The magnitude of the Coriolis term was the greatest and it was also the most variable among the terms, while the magnitude of the time partial derivative term as well as the term involving the mean relative vorticity were the smallest. The spatial structure of the mean of the Coriolis term (Figure S2 in Supporting Information S1) shows that it becomes smaller toward the shore, which was an indication that the v velocity component reduced toward shore. A similar trend was observed in the partial time derivative term. In the case of the gradient of the mean kinetic energy, there is a distinct spatial trend as peak values were observed in the southern and northeastern regions. These indicated regions of significant low frequency processes. Unlike the gradient of the mean kinetic energy, the spatial structure in the gradient turbulent kinetic energy did not exhibit a clear pattern. Also, the spatial pattern of the mean of the terms involving the mean and turbulent vorticity did not exhibit a clear pattern. Based on the standard deviations of the individual terms, the least and most variable terms are the terms involving the turbulent vorticity and the Coriolis term, respectively. Regions of highest variability for the Coriolis term are the north and southeast. Unlike the Coriolis term, the other terms were most variable in the north-western part of the region.

The structure of the spatial mean and standard deviations of the terms in the across-shelf momentum had some similarities and differences when compared to those from the along-shelf momentum. Similar to the along-shelf momentum equation, the magnitude of the mean Coriolis term was the largest as well as the most variable. Additionally, the gradient of the turbulent kinetic energy term was also the least variable as in the along-shelf momentum equation. Besides the partial time derivative term whose variability also increased toward the southeast, the

Table 1
Mean and Standard of the Along-Shelf and Across-Shelf Momentum Components Computed in Time at Each Grid Point and the Variability Across the HFR Domain of Each Statistic Is Given by the Corresponding ± Standard Deviation

		(Units: 10^{-7} ms^{-2})	
	Terms	Mean	Standard deviation
Along-shelf Momentum Components			
Partial time derivative of velocity	$\frac{\partial \bar{u}}{\partial t}$	0.0 ± 0.1	16.5 ± 3.4
Mean vorticity	$\overline{-\xi \bar{v}}$	−0.0 ± 0.7	7.0 ± 1.7
Coriolis	$-f\bar{v}$	14.3 ± 7.1	66.4 ± 4.0
Turbulent vorticity	$\overline{-\xi' v'}$	0.5 ± 0.7	5.4 ± 1.2
Gradient of turbulent kinetic energy	$\frac{1}{2}\frac{\partial \overline{u'.u'}}{\partial x}$	−0.3 ± 1.2	6.1 ± 2.3
Gradient of the mean kinetic energy	$\frac{1}{2}\frac{\partial \bar{u}.\bar{u}}{\partial x}$	−0.5 ± 1.3	8.4 ± 3.7
Divergence of stress tensor	$-\frac{\partial \tau_x}{\partial z}$	8.5	34.9
Across-shelf momentum components			
Partial time derivative of velocity	$\frac{\partial \bar{v}}{\partial t}$	0.0 ± 0.1	13.2 ± 0.8
Mean vorticity	$\overline{-\xi \bar{u}}$	1.0 ± 2.0	11.1 ± 4.3
Coriolis	$f\bar{u}$	5.5 ± 16.4	95.2 ± 19.2
Turbulent vorticity	$\overline{\xi' u'}$	1.3 ± 1.5	7.2 ± 3.3
Gradient of turbulent kinetic energy	$\frac{1}{2}\frac{\partial \overline{u'.u'}}{\partial y}$	−0.7 ± 1.1	6.0 ± 2.2
Gradient of the mean kinetic energy	$\frac{1}{2}\frac{\partial \bar{u}.\bar{u}}{\partial y}$	−0.4 ± 1.3	8.1 ± 3. 0
Divergence of stress tensor	$-\frac{\partial \tau_y}{\partial z}$	−0.1	34.1

spatial structure of the standard deviation of all the terms showed that the variability in the terms increased toward the northwest. Unlike the along-shelf momentum equation, the term with the least magnitude was the stress term. Considering the spatial structure of the mean of the terms (Figure S4 in Supporting Information S1), the Coriolis term decreased from the north toward the south of the domain. A similar structure was observed in the time derivative term. The gradient in mean kinetic energy showed an unexpected structure as it decreased from the north and south and toward the center of the domain. The mean of the gradient of the turbulent kinetic energy showed a different pattern that increased toward the north and southeast regions. Both spatial structures of the terms involving the mean and turbulent vorticity showed that the mean of the terms increased toward the west.

The importance of non-linear terms with respect to the Coriolis term was further determined from the computation of R_o. From the computations, the number of cases for which $R_o > 0.1$ was <1% of the total number of computations in space and time (17125919) in both the along-shelf and across-shelf momentum. This implies that the geostrophic balance Equation (1) can be considered as the dominant dynamical balance in the MSB for surface velocity.

4.2. Variability in the Vertical Range of MSB Sea Level Anomalies

Over the study period, the spatial variation in the vertical range in the reconstructed sea level anomalies was between 0.01 and 0.50 m. The minimum spatial range occurred on 17 November 2016 while the maximum spatial range was on 10 October 2018. A spatial range of 0.50 m is not typical for the region as the mean spatial range was estimated to be 0.12 ± 0.06 m, however because of mesoscale features such as eddies, which sporadically approach the region (e.g., Ohlmann et al., 2001, Plate 4a), larger ranges can occur.

4.3. Validation of MSB Sea Level Anomalies

The S3 SSHA data was adopted to check the fidelity of the Least Squares technique in estimating sea level anomalies. Using the cost function, anomalies in sea level were estimated from the raw hourly surface currents data

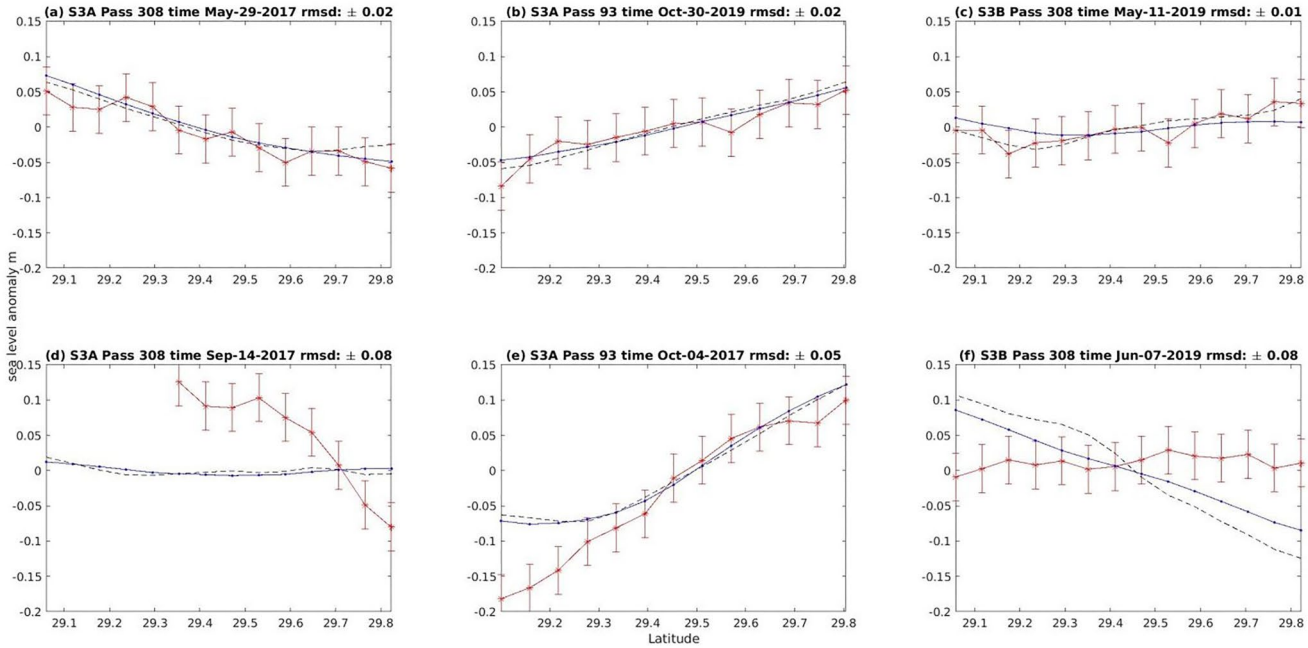

Figure 2. S3A and S3B SSHA (red solid line with error bars of 3.4 cm), HFR SSHA estimated using geostrophic approximation (blue solid line with dots) and invariant form of the momentum equations applied to raw surface currents (blue dash line) and root mean square difference between S3 and HFR SSHA (from raw surface currents) (rmsd). Instances of agreement and disagreement between S3 and HFR SSHA are shown in panels a–c and d–f, respectively.

using the invariant form of the momentum equation, which is similar to Equation (1) but ignoring the perturbation terms. As speculated in Roesler et al. (2013), the resulting HFR SSHA was expected to be relatively comparable to the SSHA from S3 as both have the contributions of HF signals. While both datasets are comparable, there were still some differences present. S3 SSHA are instantaneous observations while the hourly surface current products from HFR are hourly mean over the hour mark (http://www.codar.com/intro_hf_currentmap.shtml). The hourly HFR surface currents contain the contributions of tidal currents while ocean tides were eliminated in the S3 SSHA using models, which may or may not accurately remove the contributions of ocean tides in the study area. There is an unknown bias in the differential sea level anomalies estimated using the cost function but it is not present in the S3 data. Therefore, for each satellite pass, the along-track mean of the S3 SSHA data was subtracted to reduce the SSHA to a zero reference. The estimated HFR SSHA from the raw and filtered surface current data were interpolated on the grid points of the S3 tracks and the spatial mean corresponding to the individual interpolated HFR SSHA were removed to also reduce the sea level anomalies to a zero reference.

Plots of 86 corresponding HFR and S3 SSHAs are shown in Figure S10 in Supporting Information S1 but few instances are shown in Figure 2. A notable difference between S3 and HFR SSHAs is the presence of grid scale oscillations in S3 SSHA (Figure 2). The spatial resolution of the HFR estimated currents (6 km) are similar to the along-track altimeter sea level resolution. However, the process of estimating sea level from currents is an integrative process and acts as a low-pass filter. The high wavenumber (grid scale) oscillations in the along-track altimeter data were also reported in (Chavanne & Klein, 2010; Roesler et al., 2013). This contributed to the root mean square differences (rmsd) between the S3 and the HFR SSHAs estimates computed from raw HFR surface currents ranging from 0.00 to 0.09 m. Accounting for the errors in S3 SSHA (3.4 cm) and HFR SSHA estimated from raw surface currents (2 cm), 64% of the computed rmsd were within the error budget of 4 cm (Figure 3a) and some instances are shown in Figures 2a–2c. A similar result was obtained when the HFR SSHA estimated using geostrophic approximation was compared to S3 SSHA for an error budget of 3.5 cm (Figure 3b). This suggests an encouraging result regarding the prospect of using the Least Squares technique in estimating anomalies in sea level. Furthermore, the result is in line with Chavanne and Klein (2010) who had previously noted an agreement between the two products (HFR SSHA estimated using raw and subinertial surface currents and satellite altimeter SSHA) but in the open ocean region where satellite altimeter data are more reliable. However, there were cases when both S3 and HFR SSHAs were out of phase (Figures 2d and 2f) and it was not surprising based on the differences in the two datasets that were previously enumerated as such, contributing to rmsd larger than the

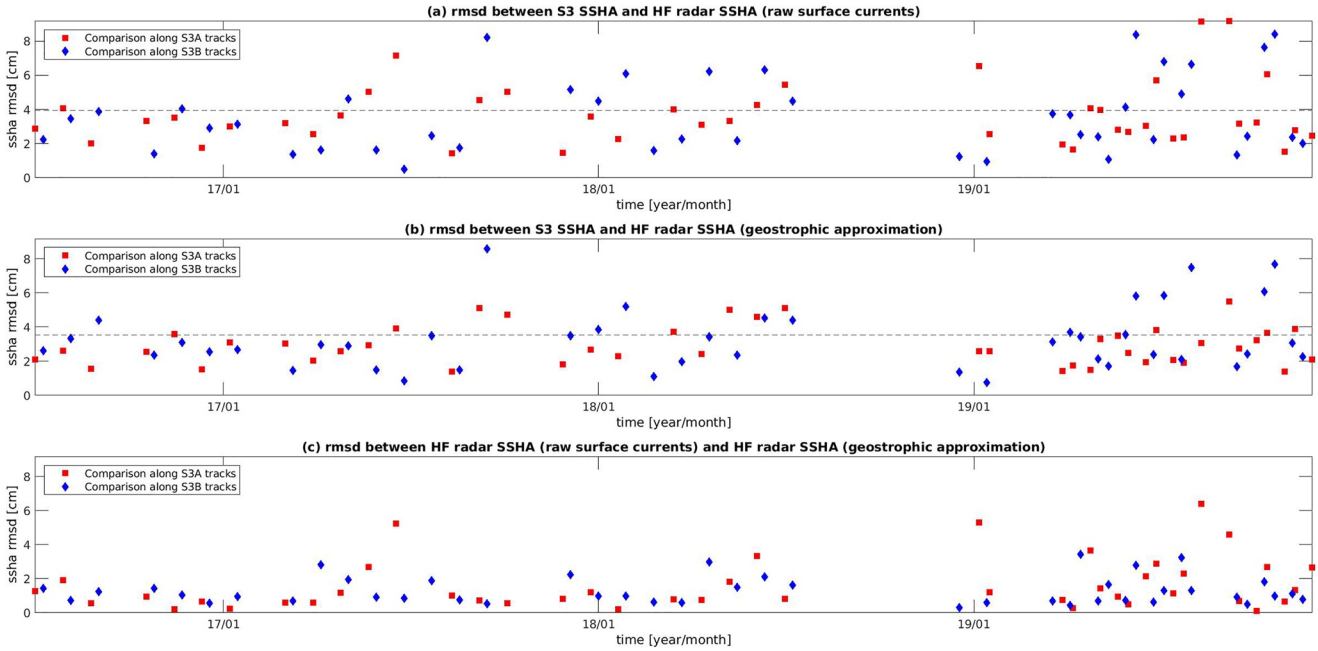

Figure 3. (a) rmsd between S3 SSHA and HFR SSHA (raw surface currents). (b) rmsd between S3 SSHA and HFR SSHA (geostrophic approximation). (c) rmsd between HFR SSHA (raw surface currents) and HFR SSHA (geostrophic approximation).

respective error budgets. Moreover, it is not unique to this study as Roesler et al. (2013) reported instances of statistically significant negative correlations in their study even after smoothing the open ocean satellite altimeter data to enhance its agreement with the HFR SSHA. Figure 2e is an instance when the rmsd was large due to the divergence of only three offshore points but there was agreement in the reminder of the points which further suggests that the differential sea level anomalies reconstructed using the Least Squares technique are reasonable.

We also compared the sea level temporal anomalies of the coastal gauge and the buoy to investigate the validity of the buoy datasets. This was done because, unlike the coastal gauge, the buoy was not stationary relative to the land. Both sea level stations were ~60 km apart. Figure 4a, shows that the magnitude of the sea level temporal anomalies at the coastal station was not always greater than the magnitude of the anomalies observed at the offshore buoy. For instance, a higher sea level anomaly observed at the buoy in October was due to Hurricane Nate as it approached the nGOM west of the buoy. Besides the contribution of the hurricane, we expected the amplitude of the sea level temporal anomalies at the coastal station to be higher, based on the influence of shoaling bathymetry on sea level amplitude (Woodworth et al., 2019). Considering that both stations were not co-located, we also expected a phase lag between the sea level temporal anomalies at the two locations. There was rather no pronounced phase lag in the sea level anomalies between the two stations. Considering a significant correlation coefficient of 0.94 at 95% confidence level between the two time series, it was safe to assume that the sea level temporal anomalies at the offshore buoy could serve as a check to the HFR SSHA.

HFR SSHA estimated from the geostrophic equation was compared with the buoy sea level temporal anomalies. Both time series were not of the same nature considering that the HFR SSHAs were with respect to a zero spatial mean while the buoy anomalies were with respect to a temporal mean. Irrespective of the different nature of the SSHA time series, we still compared the two. Firstly, a new HFR SSHA time series was generated from the centered spatial average of four HFR SSHA grid points in the vicinity of the buoy where the center of the average region was ~20 km from the buoy location. Secondly, the temporal mean of the resulting HFR SSHA time series was computed. By subtracting the temporal mean of the HFR SSHA, it became slightly more consistent with the buoy sea level temporal anomalies. We did not anticipate high correlations coefficients between the two SSHAs. It was rather surprising that the correlation coefficient and rmsd between the buoy and HFR SSHA were 0.80 ($p < 0.05$) and 0.08 m, respectively. Figure 4b further shows the similarities between these two time series as they were individually subtracted from the coastal sea level time series. .

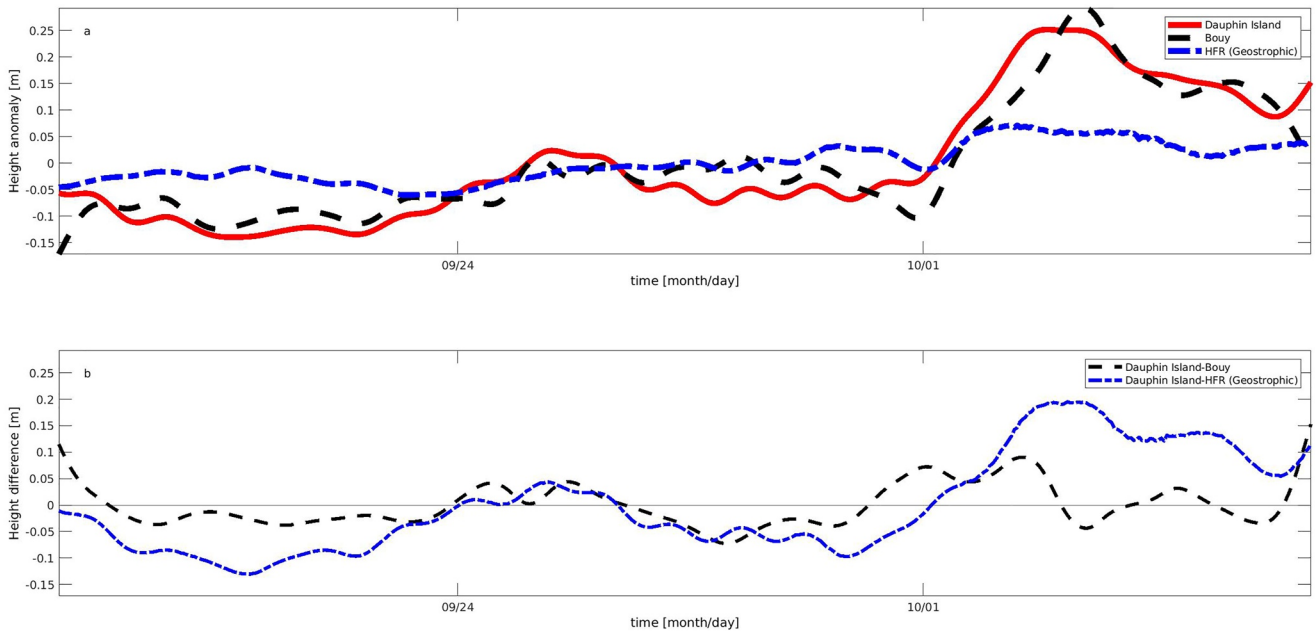

Figure 4. (a) SSHA from 2017/9/18 to 2017/10/06 NOAA coastal sea level gauge 8735180 Dauphin Island (solid line) and offshore buoy (dashed line), and HFR estimates using geostrophic (dashed line and dot) from the nearest grid point to the buoy location. (b) SSHA differences between the coastal sea level gauge and offshore buoy (dashed line), and between the coastal sea level gauge and the same HFR estimates as in (a).

4.4. EOF Modes and Momentum Equation Terms Diagnostics

Figure 5 shows the first two empirical modes and their corresponding principal components. Both empirical modes explained 85% of the spatiotemporal variability in the HFR SSHA. The first mode accounts for 47% of the variability in the HFR SSHA while the second mode accounts for 38% of the variability. The first mode shows that SSHA in the MSB slopes down toward offshore when the principal component is positive and toward the coast when the principal component is negative. In the case of the second mode, SSHA slopes down toward the west when the principal component is positive and toward the east when the principal component is negative. In the original principal component plots for the respective modes, patterns were not obvious due to HF oscillations. They were both filtered using a window of 1 month to reveal the more energetic low frequency signals (Figure 5). Mode 1 principal component appears to have a periodicity of about 6 months in the first year between March 2016 and February 2017; it was positive in spring and fall but negative in summer and winter. Between March 2017 and February 2018, the pattern of the principal component was similar as in the previous year except for spring season, which was partly positive and partly negative. Due to the presence of gaps, the pattern of mode 1 principal component could not be adequately determined for the period between March 2018 and February 2019. It did however show that the principal component was positive in spring and tended toward negative in the summer as in the first year. The remaining record of the principal component resembled the second year as it was partly positive and partly negative in the spring, negative in the summer and mostly positive in the fall. The maximum magnitude of the principal component was in the fall of 2019. Unlike the mode 1 principal component, there was no obvious pattern in the mode 2 principal component. The magnitude of the principal component of mode 2 was mostly less than the magnitude of mode 1 and its maximum magnitude was in fall 2019. When the two principal components are in-phase (for instance: summer 2016 and 2017), the slope of sea level will be in the northeast-southwest orientation. This orientation changes to the northwest-southeast when the principal components are about 180° out of phase (for instance: winter 2017, winter 2018, spring, summer and fall 2019).

5. Discussion

HFR data was fundamental in the analysis carried out in this study. While other studies in the MSB used depth integrated flow estimated using data from ADCP to study the circulation in the MSB, this study used surface flow estimated from HFR data to diagnose the terms in the momentum equation, estimate SSHA and the leading

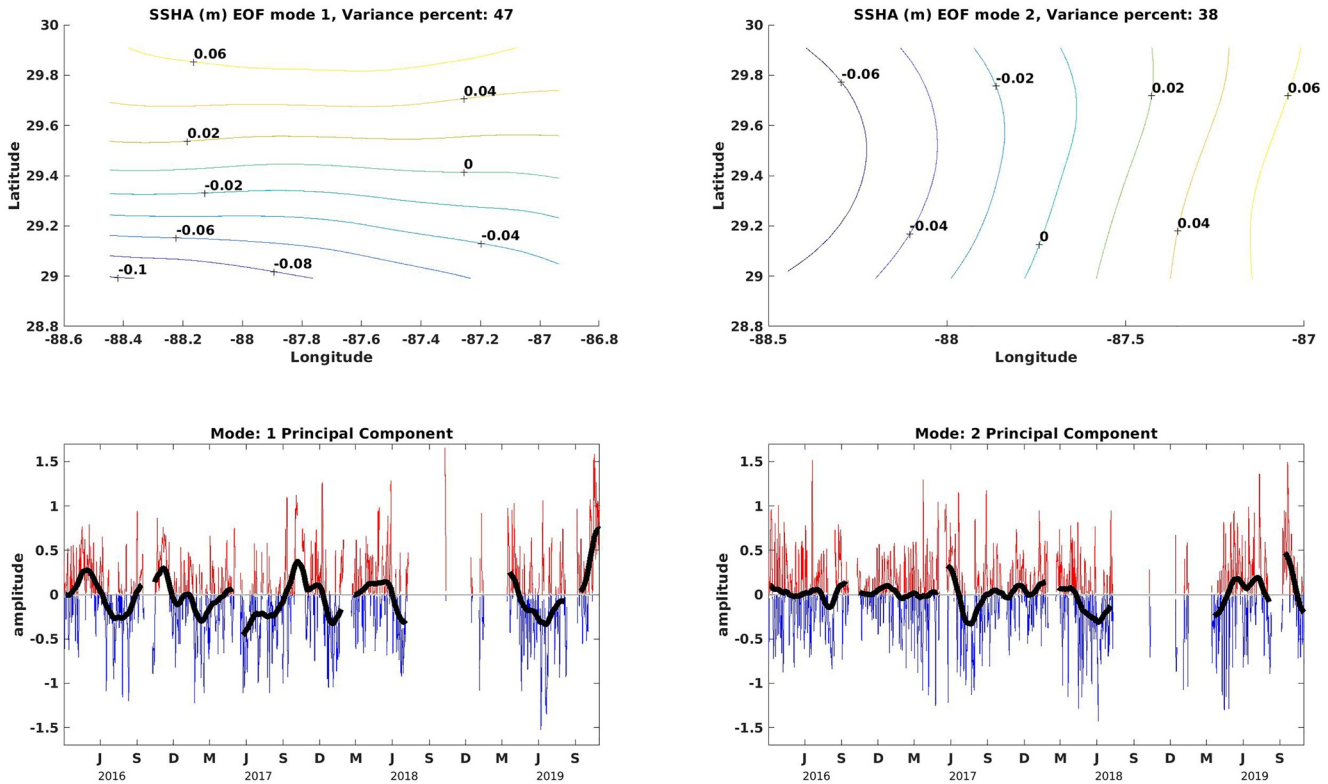

Figure 5. First two empirical modes of the HFR SSHA (top plots) and 1-month window box-car filtered principal components of the first two empirical modes where the various seasons were represented in the horizontal axis: winter (December–February), Spring (March–May), Summer (June–August), and Fall (September–November) (bottom plots).

modes in the SSHA variability. The major drawback in the MSB HFR long-range data was the presence of both temporal and spatial data gaps. Nearest neighbor and Gauss Markov estimator interpolation techniques were adopted in filling 67% of the data gaps. If there was redundancy in the number of HFR observing stations, it might not only mitigate data gaps resulting from system mal-functioning but also data gaps resulting from environmental hazards such as Hurricanes. It is believed that with redundancy in HFR observing stations, the data gaps will be negligible and could be filled using an adequate interpolation technique. Furthermore, with redundancy in the HFR stations, there will be a better quality assurance in the resulting surface currents radial and vector data.

Using the available HFR and wind data, diagnostics of the terms in the momentum equation was conducted to determine if the geostrophic balance terms were dominant at the subinertial time scales in the MSB. Results of the diagnostics showed that the Coriolis term was dominant in both the along-shelf and across-shelf momentum equations, as the $R_o < 0.1$ prevailed in the domain. Consequently, the sea level gradient terms will balance the Coriolis term implying that geostrophic balance is dominant. A similar balance was found in the across-shelf momentum equation of the West Florida Shelf by Liu and Weisberg (2005). Liu and Weisberg (2005) using depth averaged momentum equations showed that the magnitudes of the Coriolis and bottom pressure gradient terms were larger compared to the other terms in the across-shelf momentum equation, and both were significantly correlated and balanced each other. Their results further indicated that when the other terms in the across-shelf momentum equation were added to the Coriolis term, the balance with the pressure gradient term slightly improved as there was about 14% and 4% increase in correlation in the nearshore (~15 m depth) and offshore (~126 m depth). Unlike the across-shelf momentum, Liu and Weisberg (2005) noted that geostrophic balance was not dominant in the nearshore region of the along-shelf momentum. However, it would become the dominant balance from ~30 m depth toward offshore as the magnitude of the Coriolis term became dominant. Thus, the results in Liu and Weisberg (2005) were consistent with the results of our study even though our analysis were based on data from the ocean surface. Considering that the magnitude of the ageostrophic terms were insignificant and could be neglected, the dynamics in the MSB can be adequately represented by geostrophic approximation.

The feasibility of obtaining reliable SSHA using a Least Squares technique was validated using SSHA from a satellite altimeter. Satellite altimeters provide HF (20 Hz) along-track sea level data. The data used in this study were the average of the HF data at 1 Hz. Unlike the satellite altimeter SSHAs, SSHAs from HFR were not from measured sea level but estimated from subinertial surface currents after the application of Least Squares technique. The interpolation of the estimated HFR SSHA along the track of the satellite and the removal of the individual along-track SSHA spatial mean resulted in consistent and relatively comparable datasets. From both products, it was deduced that the MSB SSHA amplitude along the satellite track, which is in the north-south orientation, is mostly less than 0.1 m. In more than half of the cases of corresponding S3 and HFR SSHA, the rmsd that resulted from the comparison of the HFR SSHA estimates (filtered (subinertial) and raw surface currents) to the SSHA from satellite altimeter were within the error budget of S3 SSHA. This was an indication that reliable SSHA for the MSB can be determined by applying the Least Squares technique to HFR data.

Instances of large rmsd do not necessarily invalidate the SSHA from either technique. Liu et al. (2012) acknowledged that the differences in measuring techniques and measured variables complicates the comparisons of both datasets. For instance, S3 provides instantaneous SSHA and if a trending signal in the domain is short-lived (<1 hr) and prevailed during the satellite overpass, the magnitude is preserved in the S3 data. However, the signal may not be dominant in the HFR SSHA given that the surface currents from the HFR are not instantaneous. This will result in a divergence between both S3 and HFR SSHA. Divergence between both S3 and HFR SSHA could result from unreliable SSHA. In events of high radar backscatter from the surface ocean (Sig0 > 14 dB) and high significant wave height (SWH > 3m) the reflected altimeter signals from the ocean surface are not reliable, hence this results in degraded satellite altimeter data (Roesler et al., 2013; Tournadre et al., 2006). The study by Roesler et al. (2013) casts doubts on the reliability of satellite altimeter data on the shelf due to the complexities of shelf processes compared to open ocean processes. Additionally, Liu et al. (2012) reported that the root mean square differences between the "geostrophic velocities" estimated from X-TRACK "a coastal satellite altimeter product" and observed velocities from HFR were not within their study error budget. However, it is not consistent with the result of this study potentially due to differences in study regions, compared variables and data sources. The HFR SSHA estimated in this study can be unreliable in cases when there are gaps present in the data especially when the gaps are near the boundary of the domain. This is another reason for redundancy in HFR stations in the region. The detailed analyses of the reason(s) for the large rmsd between the S3 and HFR SSHA is beyond the scope of this study as there is no sufficient data.

SSHAs determined using the geostrophic balance approximation and the invariant form of the momentum equations provided some insights on the dominance of geostrophic balance. If the other terms in the invariant form of the momentum equation besides the Coriolis and pressure gradient terms, are significant then when they are included in the estimation of MSB SSHA the resulting SSHA should differ significantly from the SSHA estimated using geostrophic approximation. Several instances that were considered confirmed that there were differences between the two HFR SSHA estimations (Figure 2). Though there were differences in the magnitude of the SSHA, in most cases, there were agreement in the trends of the two SSHA estimates, which resulted in small values of the computed rmsd (Figure 3c). It implies that even at scales less than the subinertial scales, geostrophic balance is important in the MSB. As such, at subinertial scales, contributions of the non-linear and time derivative terms to sea level gradient can be ignored in the MSB. Consequently, the estimation of MSB SSHA from geostrophic approximation is reasonable. The major drawback in using this balance is inability to observe finer details in the MSB dynamics.

Based on the principle of geostrophy, high pressure (sea level) is to the right of geostrophic currents in the northern hemisphere. The first EOF mode of the SSHA reveals that the currents in the MSB were majorly in the east-west orientation hence the north-south sea level gradient. This is consistent with the mode 1 of the surface currents reported in Ohlmann and Niiler (2005). Coincidentally, we both reported the same percentage of energy for mode 1. Surface currents variance ellipses for the region from other sources (Hode, 2019; Ohlmann et al., 2001) showed the currents are mostly along the east-west orientation which is similar to the orientation of the bathymetry of the region. The orientation of the currents changes to the north-south based on the SSHA mode 2. This was partly consistent with the mode 2 reported in Ohlmann and Niiler (2005) which not only had a north-south component but also an east-west component.

The results of our study did not entirely agree with the results of previous studies. We assume that the discrepancies with some of the studies stems from differences in techniques as well as prevailing conditions. He and Weisberg (2003), reported that the mean currents for the spring of 1999 flowed toward the east. Though our result

showed that there was no preferred current direction in spring 2017 and 2019, it also showed that currents flowed toward the west in spring of the other years. Their analysis focused on model result depth-averaged currents, which corresponded to the mid-depth currents unlike our analysis that involved only HFR surface currents. Additionally, while our data is insufficient (~4 years) to draw a statistical conclusion on the nature of the flow for the various seasons, we had more statistics compared to analysis based on a single season. We suspect that the eastward flow in the spring that was also reported by Dzwonkowski and Park (2010) was because their analysis was based on depth averaged velocities. However, based on the velocity profiles for the spring season (Dzwonkowski & Park, 2010 Figure 4), it appears that the surface velocities tended toward the west as well as surface velocities for the other seasons. While the surface velocities reported in Dzwonkowski and Park (2010) were consistent with our results in some season, other seasonal study focused around this site showed temporal and spatial variability in the surface currents attributed to the close association with Mobile Bay estuarine discharge (Dzwonkowski et al., 2014; Dzwonkowski & Park, 2012). It did not correspond to the surface currents reversal reported in Ohlmann and Niiler (2005) thus, the misrepresentation of the surface currents likely resulted from poor extrapolation. A better comparison to our results are the studies conducted by Morey et al. (2003) and Ohlmann and Niiler (2005) using drifters and by Hode (2019) using HFR. The dataset used by Morey et al. (2003) and Ohlmann and Niiler (2005) has some overlap hence, we could expect some similarities in results. The same applies to the data used in Hode (2019) and our study. In Morey et al. (2003), westward flow reported for the winter season was not consistent with our result, however, the eastward flow in the summer season was consistent with our result. Monthly mean velocities reported in Ohlmann and Niiler (2005) were also not entirely consistent with the results reported in Morey et al. (2003) as currents were mostly toward the west in January, February and August, toward the east in July and no preferred direction in June and December. Ohlmann and Niiler (2005) also showed that there were no preferred current direction in the spring thus, not consistent with He and Weisberg (2003). Our results for the fall season are in agreement with Ohlmann and Niiler (2005) except for September where they showed that there was no preferred current direction. When compared to the monthly climatology of the surface currents reported in Hode (2019), our result are consistent for the fall and summer seasons. The results are largely consistent with the winter seasons except for December when there was no preferred current direction. In spring, Hode (2019) reported that currents flowed toward the west in March but had no preferred direction in April and May. Our results and the result of previous studies support our assumption that geostrophic balance is the dominant balance in the MSB. The details of the physical processes involved with the anomalies in geostrophic sea level are beyond the scope of this study.

6. Conclusions

From the diagnostics of the terms in the momentum equation, it was noted that geostrophic balance was the dominant balance at subinertial scales, hence other terms in the momentum equation can be neglected. Furthermore, the study highlighted the benefits of having HFR stations along the coast as the data can be used to describe circulation of a domain as well as the subinertial sea level changes. The mapped sea level anomalies over the HFR coverage in the MSB were estimated using a novel technique involving Least Squares. This is the first high resolution (temporal and spatial) mapped sea level estimates over the MSB, other than the gridded sea level estimates derived from coarse (spatial and temporal) satellite altimetry data. Ohlmann et al. (2001) argued that using SSHA data from satellite altimetry, viable information such as shelf rise flow due to eddies at the shelf rise can be obtained. They further stated that the data could be assimilated in models and also used to validate models. The results of this project provides similar oceanographic outputs to satellite altimetry but at better temporal and spatial resolutions. Though the along-track satellite altimeter has an equivalent along-track spatial resolution, it does not adequately provide 2-dimensional spatial information of oceanographic processes such as eddies. Consequently, SSHA from the HFR can be used to effectively validate SWOT altimeter data. The major drawback in using HFR SSHA is the unknown time dependent vertical offset. In future studies, a survey grade buoy will be deployed in the domain of the HFR coverage to estimate absolute HFR SSHAs.

Appendix A: Gauss Markov Interpolation

Gauss-Markov interpolation technique is the statistical approach (Drygas, 1983) utilizing correlation between observed (data) and missing values (data gaps). Missing values are recovered according to Equation (A1):

$$U' = R_{ud} R_{dd}^{-1} d' \quad \text{(A1)}$$

where R_{ud} is covariance matrix describing the covariance between unknown velocity and data, R_{dd} is covariance matrix describing the data covariance. Both matrices were built under the assumption of isotropicity and homogeneity. d' is data deviation from the mean field and u' is velocity anomaly with respect to the mean at the location of data gap. A simple Gaussian model for isotropic and homogenous correlation function was fitted to the mean covariance matrix estimated from the observed data. Kim (2010) adopted similar approach. The correlation function model was assumed to be isotropic and homogeneous in both time and space Equation (A2):

$$Rdd^{-1} = \left(0.5\left(e^{-\left(\frac{r^2}{\delta^2}\right)}e^{-\left(\frac{\tau^2}{T^2}\right)}\right) + 0.5\right). \tag{A2}$$

where r and τ are the spatial and temporal distances, respectively, between the gap grid point and the grid point of available data while δ (3.6 and 4.72 km for respective u and v velocity components) and T (4 hr for time) are the typical correlation scales in space and time respectively. Due to the magnitude of data gaps leading to insufficient statistics, some gaps remained even after the interpolation processes.

Appendix B: Correlation Between Wind Data

Wind speed and direction from the wind data were converted from meteorological direction convention (direction wind comes from) to oceanography direction convection (direction wind is flowing toward) using (http://colaweb.gmu.edu/dev/clim301/lectures/wind/wind-uv) to estimate wind velocity vectors. Complex correlations using Kundu (1976) Equation (B1) between the wind data at the various stations were calculated for the entire time series

$$r = \frac{< u_1u_2 - v_2v_1 >}{< u_1^2 + v_1^2 >^{1/2} < u_2^2 + v_2^2 >^{1/2}} + i\frac{< u_1v_2 - u_2v_1 >}{< u_1^2 + v_1^2 >^{1/2} < u_2^2 + v_2^2 >^{1/2}} \tag{B1a}$$

$$\alpha_{av} = \tan^{-1}\frac{< u_1v_2 - v_1u_2 >}{< u_1u_2 + v_1v_2 >} \tag{B1b}$$

where r is the correlation coefficient, (u_1, v_1) are the components for vector 1 which serves as the reference, (u_2, v_2) are the components for vector 2, α_{av} is the average phase angle between the vectors 1 and 2, $i = \sqrt{-1}$ and < > denotes averaging over a time period which in our case corresponded to the entire time series period. Based on table B1, the smallest correlation coefficient between the wind stations was 0.66% and it was between the furthest stations. Correlation coefficients between the other stations were above 0.7, which indicated that wind was well correlated and had relatively insignificant variability for the region. Wind data from station 42012h was adopted as the optimal wind data as it not only correlated best with the wind stations but also had the second least gaps after dpia1h. Gaps in the optimal wind data were filled using wind data from station 42040h and if the data was also missing then data from dpia1h was used while correcting for vector rotation using Equation (B2).

$$\mathrm{OWD} = (u + iv)e^{i\alpha_{av}} \tag{B2}$$

Table B1
Relative Correlation Coefficients and Angle (rad) Between Wind Stations

Correlations coefficient between wind stations of the total time series				
Wind stn	42012	42039	42040	dpia1
42012	1	0.72, 0.64	0.84, −0.53	0.86, +3.92
42039	0.72, −0.64	1	0.79, −3.32	0.66, +3.57
42040	0.84, +0.53	0.79, +3.32	1	0.77, +5.27
dpia1	0.86, −3.92	0.66, −3.57	0.77, −5.27	1

where OWD means optimal wind data, (u, v) are velocity components from wind stations 42040h or dpia1h, e is exponential, α_{av} is the average phase angle between wind station 42012h and wind station (42040h or dpia1h) and $i = \sqrt{-1}$.

Appendix C: Estimation of Boundary Layer Depth

In the open ocean the boundary layer depth (d) can be approximated by the thickness of the Ekman layer. However, the Ekman layer as proposed in Ekman (1905) is idealistic as suggested by Cushman-Roisin and Beckers (2012) based on several simplistic assumptions; for instance the assumption of a constant eddy viscosity coefficient in a geophysical flow with vertical shear and the assumption of a homogenous density of the fluid. Monin and Yaglom (1971) proposed an eddy viscosity coefficient for the estimation of the Ekman layer, which is also constant within the boundary layer but the value of the coefficient depends on the kinematics of the fluid property compared to that of Ekman (1905). A different empirical estimate of the Ekman layer that depends on wind was used in this study. With wind as the main source of turbulence in the surface ocean, the vertical length scale of the Ekman layer was parameterized by the scaled turbulence wind mixing layer in Equation (C1) (Cushman-Roisin & Beckers, 2012; Oyarzún & Brierley, 2019; Stigebbrandt, 1985).

$$d = \gamma \frac{\mathrm{u}_*}{\mathrm{f}} \tag{C1}$$

where γ is the coefficient of proportionality (0.1), f is Coriolis parameter and $\mathrm{u}_* = \sqrt{|\tau|}$ is the turbulent friction velocity. This parameterization of the Ekman layer does not account for the overlap of both the surface and bottom boundary layers and the effect of stratification. Despite these challenges, this parameterization has been used in other studies. Different values of γ were adopted in previous studies. Modjeld and Lavelle (1984) and Stigebbrandt (1985) suggested the value of γ to be ~0.2 while Cushman-Roisin and Beckers (2012) and Oyarzún and Brierley (2019) suggested the value of 0.4. We took a deterministic approach toward the selection of the coefficient γ. The depth of boundary layer decreases due to vertical stratification (Cushman-Roisin & Beckers, 2012) since more wind energy is spent mixing stratified fluid. As such, the boundary layer depth should closely resemble the mixed layer depth. Time series of boundary layer depth were computed for various values of γ. The seasonal cycle of the estimated boundary layer depth was compared to the estimate of the annual variations of the mixed layer depth in (Zavala-Hidalgo et al., 2014) and the value γ at which the boundary layer depth closely resembles the mixed layer depth was determined to be 0.1. When the estimated boundary layer depth exceeds the 0.8 of the bathymetry (e.g., in shallower region), we assume the boundary layer depth to be equal to 0.8 of the bathymetry. The application of the boundary layer depth correction procedure was limited to a region in the inner shelf. The correction procedure was applied in relatively few occasions in time for increased turbulent friction velocity. Despite the exaggeration of the last term in Equation (1) that resulted from a lower value (0.1) of γ, the correction procedure is not critical in this study as the term that was approximated was not the leading term in the momentum balance.

Conflict of Interest

The authors declare no conflicts of interest relevant to this study.

Data Availability Statement

The data used in this study are publicly available and their sources are thus: https://cordc.ucsd.edu/projects/mapping/maps/, https://www.aviso.altimetry.fr/en/home.html?id=611&L=0 and https://tidesandcurrents.noaa.gov/map/, https://www.ndbc.noaa.gov/. Offshore GNSS data has been uploaded to Unavco.

Acknowledgments
Funding for this project was through award NA18NOS0120018 to the Gulf of Mexico Coastal Ocean Observing System from the Integrated Ocean Observing System Office of the National Oceanic and Atmospheric Administration. We appreciate the hard work of the CenGOOS group at USM towards keeping the HFR stations operational and their diligence in making the data available. Furthermore, we appreciate the contributions of Dr. Umezuruike Sunday and Dr. Asper Vernon as their inquiries and comments improved the readability of the manuscript. Furthermore, we thank Dr. Dan Codiga and Dr. Laurent Roblou for their contributions. We thank the reviewers of the manuscript for their very helpful comments.

References

Andersen, O. B., & Scharroo, R. (2011). In S. Vignudelli, A. Kostianoy, P. Cipollini, & J. Benveniste (Eds.), *Range and geophysical corrections in coastal regions: And implications for mean sea surface determination*. Springer Berlin Heidelberg.

Bisnath, S., Wells, D., Santos, M., & Cove, K. (2004). Initial results from a long baseline, kinematic, differential GPS carrier phase experiment in a marine environment. 26–29.

Björnsson, H., Venegas, S. a., Bjornsson, H., & Venegas, S. a. (1997). A manual for EOF and SVD analysis of climatic data. *CCGCR Report*, *97*(97), 52. https://doi.org/10.1002/elps.200700001

Bonnefond, P., Laurain, O., Exertier, P., Boy, F., Guinle, T., Picot, N., et al. (2018). Calibrating the SAR SSH of sentinel-3A and CryoSat-2 over the corsica facilities. *Remote Sensing*, *10*(1), 1–14. https://doi.org/10.3390/rs10010092

Bretherton, C. (2002). Atmospheric Science 547 boundary layer meteorology.

Chapman, R. D., & Graber, H. C. (1997). Validation of HF radar measurements. *Oceanography*, *10*(SPL.ISS. 2), 76–79. https://doi.org/10.5670/oceanog.1997.28

Chavanne, C. P., & Klein, P. (2010). Can oceanic submesoscale processes be observed with satellite altimetry? *Geophysical Research Letters*, *37*(22), 2. https://doi.org/10.1029/2010GL045057

Chelton, D. B., Deszoeke, R. A., Schlax, M. G., Elnaggar, K., & Siwertz, N. (1998). Geographical variability of the first baroclinic Rossby radius of deformation. *Journal of Physical Oceanography*, *28*(3), 433–460. https://doi.org/10.1175/1520-0485(1998)028<0433:GVOTFB>2.0.CO;2

Chelton, D. B., Ries, J. C., Haines, B. J., Fu, L. L., & Callahan, P. S. (2001). Chapter 1 satellite altimetry. *International Geophysics*, *69*(C), 1–131. https://doi.org/10.1016/S0074-6142(01)80146-7

Cho, K., Reid, R. O., & Nowlin, W. D. (1998). Objectively mapped stream function fields on the Texas-Louisiana shelf based on 32 months of moored current meter data. *Journal of Geophysical Research*, *103*(C5), 10377–10390. https://doi.org/10.1029/98jc00099

Christensen, E. J., Haines, B. J., Keihm, S. J., Morris, C. S., Norman, R. A., Purcell, G. H., et al. (1994). Calibration of TOPEX/POSEIDON at platform harvest. *Journal of Geophysical Research*, *99*(C12), 24465. https://doi.org/10.1029/94jc01641

Cushman-Roisin, B., & Beckers, J.-M. (2012). In R. Dmowska, D. Hartmann, & T. Rossby (Eds.), *Introduction to geophysical fluid dynamics: Physical and numerical aspects* (2nd ed.). Academic Press.

Drygas, H. (1983). Sufficiency and completeness in the general Gauss-Markov model by. *The Indian Journal of Statistics, Series A (1961-2002)*, *45*(1), 88–98. https://doi.org/10.1177/0008068319570201

Dzwonkowski, B., Kohut, J. T., & Yan, X. H. (2009). Seasonal differences in wind-driven across-shelf forcing and response relationships in the shelf surface layer of the central mid-Atlantic bight. *Journal of Geophysical Research*, *114*(8), 1–15. https://doi.org/10.1029/2008JC004888

Dzwonkowski, B., & Park, K. (2010). Influence of wind stress and discharge on the mean and seasonal currents on the Alabama shelf of the northeastern Gulf of Mexico. *Journal of Geophysical Research*, *115*(12), 1–11. https://doi.org/10.1029/2010JC006449

Dzwonkowski, B., & Park, K. (2012). Subtidal circulation on the Alabama shelf during the Deepwater Horizon oil spill. *Journal of Geophysical Research*, *117*(3), 1. https://doi.org/10.1029/2011JC007664

Dzwonkowski, B., Park, K., Lee, J., Webb, B. M., & Valle-Levinson, A. (2014). Spatial variability of flow over a river-influenced inner shelf in coastal Alabama during spring. *Continental Shelf Research*, *74*(January 2013), 25–34. https://doi.org/10.1016/j.csr.2013.12.005

Ekman, V. W. (1905). On the influence of the earth's rotation on ocean-currents. Retrieved from https://jscholarship.library.jhu.edu

He, R., & Weisberg, R. H. (2003). West Florida shelf circulation and temperature budget for the 1998 fall transition. *Continental Shelf Research*, *23*(8), 777–800. https://doi.org/10.1016/S0278-4343(03)00028-1

Hode, L. (2019). *Establishing the role of the Mississippi-Alabama barrier islands in Mississippi sound and bight circulation using observational data analysis and a coastal model*. The University of Southern Mississippi.

Kim, S. Y. (2010). Observations of submesoscale eddies using high-frequency radar-derived kinematic and dynamic quantities. *Continental Shelf Research*, *30*(15), 1639–1655. https://doi.org/10.1016/j.csr.2010.06.011

Kundu, P. K. (1976). Ekman veering observed near the ocean bottom. *Journal of Physical Oceanography*, *6*(2), 238–242. https://doi.org/10.1175/1520-0485(1976)006<0238:evonto>2.0.co;2

Large, W. G., & Pond, S. (1981). Open ocean momentum flux measurements in moderate to strong winds. *Physical Oceanography*, *11*(3), 324–336. https://doi.org/10.1175/1520-0485(1981)011<0324:oomfmi>2.0.co;2

Lentz, S. J., & Fewings, M. R. (2012). The wind- and wave-driven inner-shelf circulation. *Annual Review of Marine Science*, *4*(1), 317–343. https://doi.org/10.1146/annurev-marine-120709-142745

Liu, Y., & Weisberg, R. H. (2005). Momentum balance diagnoses for the West Florida shelf. *Continental Shelf Research*, *25*(17), 2054–2074. https://doi.org/10.1016/j.csr.2005.03.004

Liu, Y., & Weisberg, R. H. (2007). Ocean currents and sea surface heights estimated across the West Florida shelf. *Journal of Physical Oceanography*, *37*(6), 1697–1713. https://doi.org/10.1175/jpo3083.1

Liu, Y., Weisberg, R. H., Merz, C. R., Lichtenwalner, S., & Kirkpatrick, G. J. (2010). HF radar performance in a low-energy environment: CODAR SeaSonde experience on the West Florida shelf. *Journal of Atmospheric and Oceanic Technology*, *27*(10), 1689–1710. https://doi.org/10.1175/2010JTECHO720.1

Liu, Y., Weisberg, R. H., Vignudelli, S., Roblou, L., & Merz, C. R. (2012). Comparison of the X-TRACK altimetry estimated currents with moored ADCP and HF radar observations on the West Florida Shelf. *Advances in Space Research*, *50*(8), 1085–1098. https://doi.org/10.1016/j.asr.2011.09.012

Madec, G., Delecluse, P., Imbard, M., & Levy, C. (1998). Institut Pierre Simon Laplace ocean general circulation model reference manual.

Mertz, F., Rosmorduc, V., Maheu, C., & Faugere, Y. (2017). For sea level SLA products. *Copernicus Marine Service*, *1.1*, 1–51. Retrieved from https://resources.marine.copernicus.eu/documents/PUM/CMEMS-SL-PUM-008-032-062.pdf

Modjeld, H. O., & Lavelle, J. W. (1984). Setting the length scale in a second-order closure model of the unstratified bottom boundary layer. *Journal of Physical Oceanography*, *14*(4), 833–839. https://doi.org/10.1175/1520-0485(1984)014<0833:stlsia>2.0.co;2

Monin, A. S., & Yaglom, A. M. (1971). *Statistical fluid mechanics (Vols. 1–2)*. MIT Press.

Morey, S. L., Martin, P. J., O'Brien, J. J., & Wallcraft, A. A. (2003). Export pathways for river discharged fresh water in the northern Gulf of Mexico. *Journal of Geophysical Research*, *108*(C10), 3303. https://doi.org/10.1029/2002JC001674

Nwankwo, U., Howden, S., Connon, B., Nechaev, D., & Wells, D. (2020). *The importance of data in analyzing the response of the circulation and sea level on continental shelf from Louisiana to Alabama to Hurricane Nate and tropical storm Alberto* (Vol. 14). Canadian Hydrographic Conference.

Nwankwo, U. C., Howden, S., & Wells, D. (2019). *Further investigations of VDatum to NAD83 vertical separations using United States geological service (USGS) coastal water levels gage and hydrolevel buoy. U.S. hydrographic conference, 1–12*. Biloxi.

Ohlmann, J. C., & Niiler, P. P. (2005). Circulation over the continental shelf in the northern Gulf of Mexico. *Progress in Oceanography*, *64*(1), 45–81. https://doi.org/10.1016/j.pocean.2005.02.001

Ohlmann, J. C., Niiler, P. P., Fox, C. A., & Leben, R. R. (2001). Eddy energy and shelf interactions in the Gulf of Mexico. *Journal of Geophysical Research*, *106*(C2), 2605–2620. https://doi.org/10.1029/1999jc000162

Oyarzún, D., & Brierley, C. M. (2019). The future of coastal upwelling in the Humboldt current from model projections. *Climate Dynamics*, *52*(1–2), 599–615. https://doi.org/10.1007/s00382-018-4158-7

Paduan, J., & Graber, H. C. (1997). Introduction to high-frequency radar: Reality and myth. *Oceanography*, *10*(2), 36–39. https://doi.org/10.5670/oceanog.1997.18

Pereira, M. B., & Berre, L. (2006). The use of an ensemble approach to study the background error covariances in a global NWP model. *Monthly Weather Review*, *134*(9), 2466–2489. https://doi.org/10.1175/MWR3189.1

Pugh, D., & Philip, W. (2014). Sea-level science understanding tides, surges, tsunamis and mean sea-level changes. https://doi.org/10.1017/CBO9781139235778

Quartly, G. D., Srokosz, M. A., & Guymer, T. H. (1998). Understanding the effects of rain on radar altimeter waveforms. *Advances in Space Research*, *22*(11), 1567–1570. https://doi.org/10.1016/S0273-1177(99)00072-1

Roesler, C. J., Emery, W. J., & Kim, S. Y. (2013). Evaluating the use of high-frequency radar coastal currents to correct satellite altimetry. *Journal of Geophysical Research: Oceans*, *118*(August 2012), 3240–3259. https://doi.org/10.1002/jgrc.20220

Rudnick, D. L., Gopalakrishnan, G., & Cornuelle, B. D. (2014). Cyclonic eddies in the Gulf of Mexico: Observations by underwater gliders and simulations by numerical model. *Journal of Physical Oceanography*, *45*(1), 313–326. https://doi.org/10.1175/jpo-d-14-0138.1

Stewart, R. H., & Joy, J. W. (1974). HF radar measurement of surface current. *Deep-Sea Research*, *21*(21), 1039–1049. https://doi.org/10.1016/0011-7471(74)90066-7

Stigebbrandt, A. (1985). A model for the seasonal pycnocline in rotating systems with application to the Baltic proper. *Journal of Physical Oceanography*, *15*(11), 1392–1404. https://doi.org/10.1175/1520-0485(1985)015<1392:amftsp>2.0.co;2

Teague, C. C., Vesecky, J. F., & Fernandez, D. M. (1997). HF radar instruments, past to present. *Oceanography*, *10*(02), 40–44. https://doi.org/10.5670/Oceanog.1997.19

Tournadre, J., Chapron, B., Reul, N., & Vandemark, D. C. (2006). A satellite altimeter model for ocean slick detection. *Journal of Geophysical Research*, *111*(4), C04004. https://doi.org/10.1029/2005JC003109

Valle-Levinson, A., & Martin, J. B. (2020). Solar activity and lunar precessions influence extreme sea-level variability in the US Atlantic and Gulf of Mexico coasts. *Geophysical Research Letters*, *40*(20). https://doi.org/10.1029/2020GL090024

Woodworth, P. L., Melet, A., Marcos, M., Ray, R. D., Wöppelmann, G., Sasaki, Y. N., et al. (2019). Forcing factors affecting sea level changes at the coast. *Surveys in Geophysics*, *40*(6), 1351–1397. https://doi.org/10.1007/s10712-019-09531-1

Yoshikawa, Y., Masuda, A., Marubayashi, K., Ishibashi, M., & Okuno, A. (2006). On the accuracy of HF radar measurement in the Tsushima Strait. *Journal of Geophysical Research*, *111*(4), 2–11. https://doi.org/10.1029/2005JC003232

Zagar, N., Andersson, E., & Fisher, M. (2004). *Based on a study of equatorial*. Weather. (April).

Zavala-Hidalgo, J., Romero-Centeno, R., Mateos-Jasso, A., Morey, S. L., & Martínez-López, B. (2014). The response of the Gulf of Mexico to wind and heat flux forcing: What has been learned in recent years? *Atmósfera*, *27*(3), 317–334. https://doi.org/10.1016/S0187-6236(14)71119-1